Supplemental information

Efficient Seawater Electrolysis for Hydrogen Production with a NiS_2 Stabilized 1T-MoS_2 Catalyst

Lianhui Wu[a], Haiying Wei[b], Hanxiao He[a], Yuwan Xiang[a], Shiyue Yin[b], Daying Guo[a]*, Guoyong Fang[a], Huile Jin[a], Xi'an Chen[a*], and Shun Wang[a]

[a]College of Chemistry and Materials Engineering, Wenzhou University, Wenzhou, China 325035.

[b]China Tobacco Jiangsu Industrial Co., Ltd., Nanjing, 210019, China

* To whom correspondence should be addressed. E-mail: guody@wzu.edu.cn; xianchen@wzu.edu.cn

Experimental Section

Chemicals

Carbon cloth (CC) was purchased from Kunshan Shengshi Jingxin New Materials Co., Ltd. (Suzhou, China). nickel nitrate hexahydrate ($Ni(NO_3)_2 \cdot 6H_2O$), sodium molybdate dihydrate ($Na_2MoO_4 \cdot 2H_2O$), ethanol, acetone, KOH and sulfur powder (S) purchased from Aladdin. All chemicals and reagents were of analytical grade and used as received. Pt/C (20wt% Pt on Vulcan XC-72R), RuO_2 (Ruthenium dioxide) and Nafion (5wt%) were purchased from Alfa Aesar. All chemicals were used as received without further purification, and all aqueous solutions were prepared with ultrapure water (>18.25 MΩ cm) obtained from a Millipore system.

Preparation of NiMoO-Pre: NiO-Pre/CC was synthesized via a hydrothermal method. In a typical procedure, 0.4834 g of $Na_2MoO_4 \cdot 2H_2O$ and 0.584 g of $Ni(NO_3)_2 \cdot 6H_2O$ are dissolved in 30 mL of ultra-pure water and stirred for 1 h to form a homogeneous solution. This solution was then transferred to a 50 mL Teflon-lined stainless steels autoclave, in which a clean carbon cloth (1 × 1.5 cm) is immersed. The autoclave is heated to 150°C for 6 h. Upon cooling to room temperature, the resulting NiMoO-Pre product is washed sequentially with ultra-pure water and ethanol and subsequently dried at 60°C overnight.

Preparation of 1TMoS$_2$-NiS$_2$/CC: A NiMoO-Pre on carbon cloth (CC) is placed in a quartz tube with 500 mg of sulfur powder and sealed. The tube is then heated at 400 °C for 120 minutes in a tube furnace to form the 1TMoS$_2$-NiS$_2$/CC electrode.

Preparation of NiS$_2$/CC: A clean carbon cloth was immersed in a solution containing 0.584 g $Ni(NO_3)_2 \cdot 6H_2O$, 0.222 g NH_4F, and 0.6 g urea dissolved in 30 mL of solvent. The mixture was subjected to hydrothermal treatment at 120°C for 6 h. After cooling to room temperature, a Ni precursor was obtained. The subsequent sulfurization process followed the same method used in the synthesis of 1T MoS$_2$-NiS$_2$/CC.

Preparation of MoS$_2$/CC: 0.4834 g of sodium molybdate dihydrate ($Na_2MoO_4 \cdot 2H_2O$) and a clean carbon cloth were added to 20 mL of deionized water. The mixture was

heated to 80°C in a water bath. Subsequently, 10 mL of HNO_3 was added, and the solution was stirred in the water bath for 3 h to obtain the Mo precursor. The sulfurization step was carried out in the same manner as the synthesis of 1T MoS_2-NiS_2/CC.

Synthesis of electrodes of Pt/C and RuO_2 on CC: Pt/C catalyst inks were prepared by mixing commercial-available Pt/C (20 wt%) in a Nafion (0.05 wt%) solution containing isopropanol (20%) and water (80%) under rigorous sonication for 0.5 h to ensure homogeneous suspension. A total of 200 μL Pt/C inks were drop-cast onto CC (1 cm × 1 cm) to prepare Pt/C electrodes for electrochemical measurements. RuO_2 electrodes were prepared by the same method.

Characterizations

The microstructures of investigated catalysts were characterized by scanning electron microscopy (SEM, FEI Quanta, Nova Nano SEM 450) and transmission electron microscopy (TEM, J Tecnai G2 F30 S-TWIN). The energy-dispersive X-ray spectrometer (EDS, Oxford) profiles of these catalysts were also collected during TEM measurements. The X-ray diffraction patterns (XRD, Rigaku TTRIII-18KW) with Cu Kα radiation (λ = 1.5406 Å) were recorded to investigate the phase composition of these catalysts in the range of 10 - 90°. The X-ray photoelectron spectroscopy (XPS, Thermo Scientific K-Alpha$^+$) measurements of these catalysts were conducted with an Al Kα source. The surface charge was corrected by referencing the spectra to the C 1s peak for the C-C bond at a binding energy of 284.8 eV.

Electrochemical active surface area (ECSA): The active surface area of each catalyst was estimated from their electrochemical capacitances, which can be measured using simple cyclic voltammetry method. The current was measured in a narrow potential window where no faradaic process was observed. We sweep the potential between 0.1 to 0.2 V vs RHE (HER) at each of Six different scan rates (10, 20, 30, 40, 50 and 60 mV s^{-1}). By plotting the difference in current density (J) between anodic and cathodic sweeps (ΔJ) at a fixed potential against the scan rate, a linear trend is observed. The fitting slope is twice of the double-layer capacitance (C_{dl}), which is linearly promotional

to the ECSA. The calculation formula is as follows:

$$ECSA = \frac{C_{dl}(catalyst)\ mF\ cm^{-2}}{C_s\ mF\ cm^{-2} \cdot per\ ECSA\ cm^{-2}}$$

Electrochemical Measurements: Electrochemical measurements were performed using a CHI 600 electrochemical workstation in a three-electrode system, with 1T MoS_2-NiS_2/CC as the working electrode, a graphite rod as the counter electrode, and an Hg/HgO electrode as the reference. Potentials were referenced to the reversible hydrogen electrode (RHE), with the relationship E(RHE) = E(Hg/HgO) + 0.059 × pH +0.098V. Current densities (j) were normalized to the geometric surface area. For comparison, RuO_2 and Pt/C were loaded on CC with the same amount as 1TMoS_2-NiS_2/CC. Polarization curves were recorded in 1.0 M KOH + 0.5 M NaCl at a scan rate of 5 mV s^{-1}, with 80% iR compensation. Electrochemical impedance spectroscopy (EIS) was carried out with a 10 mV AC amplitude at frequencies from 100 kHz to 0.1 Hz. Water splitting was evaluated in a two-electrode system using the same solution, with polarization curves measured at 5 mV s^{-1}.

In situ Raman measurement: In situ Raman spectra were acquired on NanoWizard equipped with a laser excitation source of 633 nm. Raman peaks were calibrated against the first-order optical phonon mode of a silicon wafer (520.7 cm^{-1}) prior to measurements. The electrochemical measurements were conducted with a CHI660E electrochemical workstation in a three-electrode configuration, where 1T-MoS_2-NiS_2/CC served as the working electrode, Ag/AgCl (saturated KCl) as the reference electrode, and a Pt wire as the counter electrode. In situ Raman spectra were recorded under applied potentials ranging from 0 to -0.5 V *vs* RHE, with 0.1 V increments.

Inductively Coupled Plasma Optical Emission Spectrometer（ICP-OES）measurements: The ICP-OES experiment, and calculated the contents of NiS_2 and MoS_2 in 1TMoS_2-NiS_2/CC as 13.7 mg/cm^2 and 11.62 mg/cm^2, respectively, according to the concentrations of Ni^{2+} and Mo^{6+} in the sample.

DFT Calculations: We have employed the first-principles to perform all density functional theory (DFT) calculations within the generalized gradient approximation (GGA) using the Perdew-Burke-Ernzerhof (PBE) formulation. We have chosen the projected augmented wave (PAW) potentials to describe the ionic cores and take valence electrons into account using a plane wave basis set with a kinetic energy cutoff of 500 eV. Partial occupancies of the Kohn−Sham orbitals were allowed using the Gaussian smearing methods with a width of 0.05 eV. The electronic energy was considered self-consistent when the energy change was smaller than 10^{-6} eV. A geometry optimization was considered convergent when the energy change was smaller than 0.03 eV $Å^{-1}$. In our structure, the U correction is used for Ni (4.9 eV) atoms. The vacuum spacing in a direction perpendicular to the plane of the structure is 20 Å for the surfaces. The Brillouin zone integration is performed using 2×2×1 Monkhorst-Pack k-point sampling for a structure. Finally, the adsorption energies (E_{ads}) were calculated as Eads= $E_{ad/sub}$-E_{ad}-E_{sub}, where $E_{ad/sub}$, E_{ad}, and E_{sub} are the total energies of the optimized adsorbate/substrate system, the adsorbate in the structure, and the clean substrate, respectively. The free energy was calculated using the equation:

$$G=Eads+ZPE-TS$$

where G, Eads, ZPE and TS are the free energy, total energy from DFT calculations, zero-point energy and entropic contributions, respectively. hydrogen spillover pathway can be calculated using the nudged elastic band (NEB) method with the transition state of an elementary reaction step. In the NEB method, the path between the reactant (s) and product (s) was discretized into a series structural.

Flow electrolytic cell measurement: Catalysts were prepared 1T MoS_2-NiS_2/CC as an cathode (loading 1.1 mg cm^{-2}), and 1.5 mg cm^{-2} of RuO_2/CC anodic on the cathode. The active area was controlled at 9 cm^2 (3 cm×3 cm). For the FCEM test, the temperature was controlled at 25°C, and alkaline seawater (Among them, the seawater

comes from Dongtou District, Wenzhou, Zhejiang, China) was kept flowing through the cell at 20 mL min^{-1}. Activation was carried out prior to the test with a prepolarization at 0.1 A cm^{-2} for1 h. The steady-state polarization curve was de-termined via the galvanostatic method, and each point was recorded until the cell voltage was stable. The stability test in FCEM ran at 10 and 100 mA cm^{-2} for 100 h. The amphoteric ionic nafion membranes used in FCEM. The treatment methods of membrane: The membrane is used directly after being immersed in the real seawater for 48 h.

The main components in various electrolytes

	Concentration of elements/ppm				PH
	Na	K	Mg	Ca	
1M KOH+0.5M NaCl	9802	27988	-	-	13.81
1M KOH + real Seawater	9795	27981	1025	263	13.74

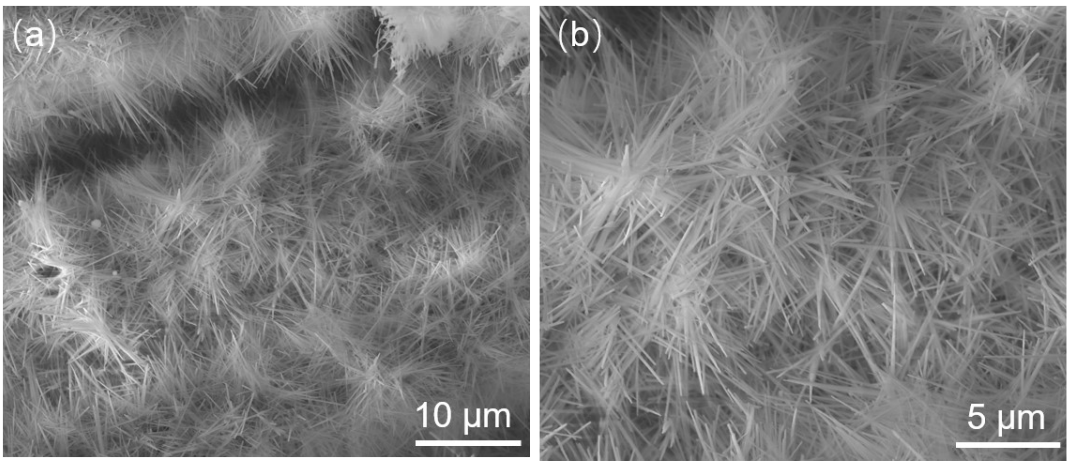

Figure S1. SEM images of NiMoO-pre/CC observed in different sizes.

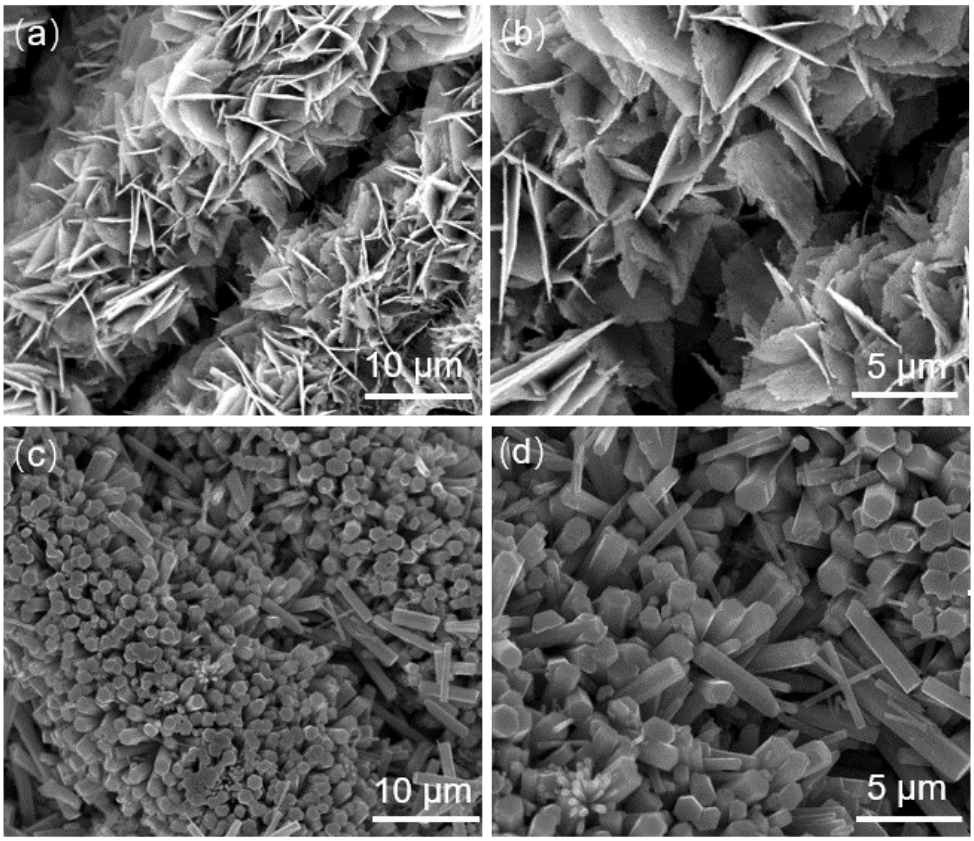

Figure S2. SEM images of (a, b) NiS_2/CC. (c, d) MoS_2/CC.

The observed g-value of 2.003 for the 1TMoS_2-NiS_2/CC sample indicates the presence of S defects. The introduction of S defects activates Mo-Mo bonds and neighboring S atoms, promoting electron transfer and accelerating proton adsorption-desorption, thereby enhancing the kinetics of the hydrogen evolution reaction.

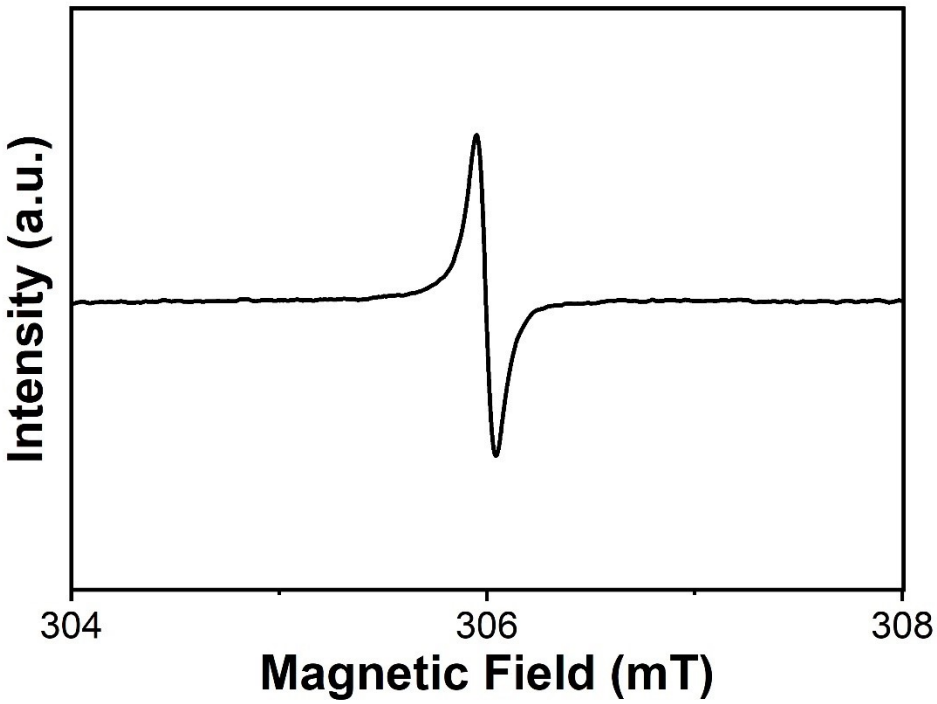

Figure S3. Electron paramagnetic resonance spectra of 1TMoS_2-NiS_2/CC.

X-ray diffraction (XRD) is employed to analyze the phase composition of 1TMoS$_2$-NiS$_2$/CC. The optimum vulcanization temperature was investigated (**Figure S4**). With the increase of temperature, the NiMo-Pre gradually changes to NiS$_2$ and MoS$_2$, and the crystallinity becomes better. It is worth noting that at 300 °C, the MoS$_2$ phase appears, but the crystallinity of NiS$_2$ is not good, but when the temperature rises to 400 °C, MoS$_2$ and NiS$_2$ are generated, and the crystallinity is just right. The sulfide phase 1T is the best when the temperature is 400℃.

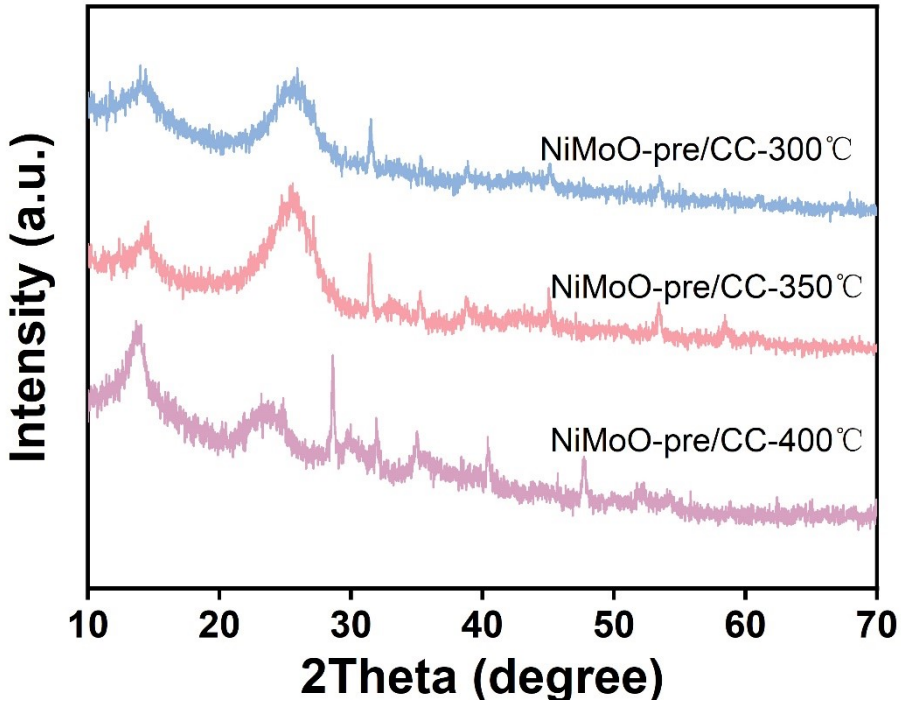

Figure S4. The XRD of 1TMoS$_2$-NiS$_2$/CC with different sulfur temperature.

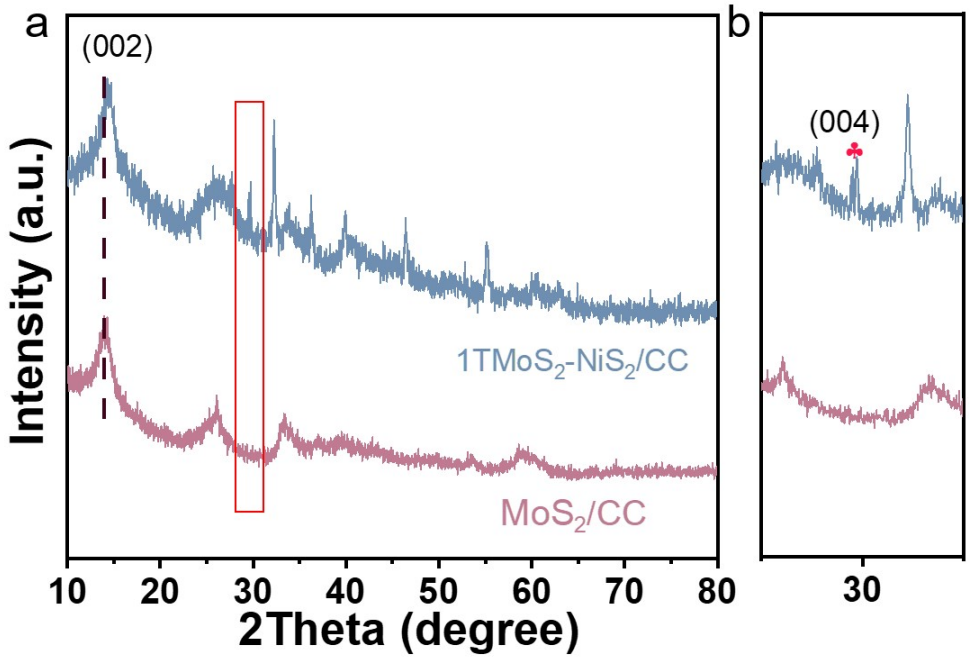

Figure S5. (a) XRD diffraction patterns of various samples. (b) The enlarged area of the red box in Figure S5a.

As shown in **Fig. 2c**, the X-ray photoelectron spectroscopy (XPS) spectrum of the synthesized catalyst confirms the presence of Mo, Ni, S, and C elements.

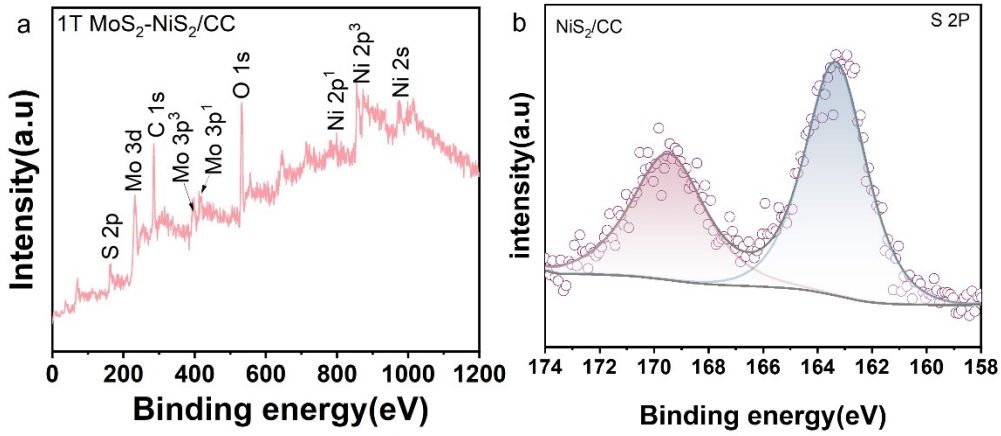

Figure S6. (a) XPS survey of 1TMoS_2-NiS_2/CC. (b) The XPS high resolution spectrogram of S 2p in NiS_2/CC sample.

As shown in **Figure 2f**, the average oxidation state of Mo species is proved by the K-edge XANES of Mo in various samples (**Figure S7a**). Apparently, the position of the 1TMoS$_2$-NiS$_2$/CC is located between Mo foil and MoS$_2$, indicating that the oxidation state of Mo is between the two references. The chemical state of Mo in 1TMoS$_2$-NiS$_2$/CC is completely different from that of MoS$_2$, which indicates that MoS$_2$ in 1TMoS$_2$-NiS$_2$/CC is partially in metallic state. Fourier transform EXAFS spectrum (FT-EXAFS) further verified the coordination of Mo in the 1TMoS$_2$-NiS$_2$/CC. From **Figure S7b**, the 1TMoS$_2$-NiS$_2$/CC exhibits an obvious Mo-S peak at 1.96 Å, which is mainly due to the scattering of Mo-S coordination. Compared with MoS$_2$, the Mo-S bond in 1TMoS$_2$-NiS$_2$/CC is obviously blue-shifted, indicating the strong electronic coupling between MoS$_2$ and NiS$_2$ in 1TMoS$_2$-NiS$_2$/CC. In addition, compared with MoS$_2$, the coordination number of S in 1TMoS$_2$-NiS$_2$/CC is close to 6 (**Table S1**), which further indicates that 1T phase is contained in 1TMoS$_2$-NiS$_2$/CC.

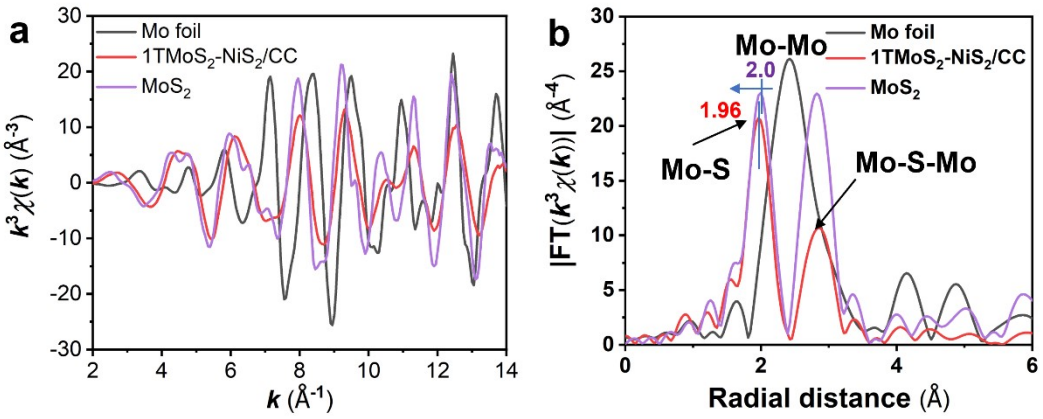

Figure S7. (a) k space fitting curve of various materials. (b) Fourier transform EXAFS spectrum (FT-EXAFS) curves of the Mo Kedge.

Notably, 1TMoS$_2$-NiS$_2$/CC exhibits performance comparable to the commercial benchmark Pt/C (20%) at current densities below 70 mA cm^{-2}, but outperforms Pt/C at higher current densities. In **Figure S8**, further compares the overpotential of the prepared catalyst at 100 mAcm^{-2}, which reflects the 1TMoS$_2$-NiS$_2$ heterojunction, and the abundant interface and defects greatly improve HER performance. This improvement is attributed to the strong electronic interactions at the heterogeneous interface, which facilitate the adsorption and dissociation of water molecules.

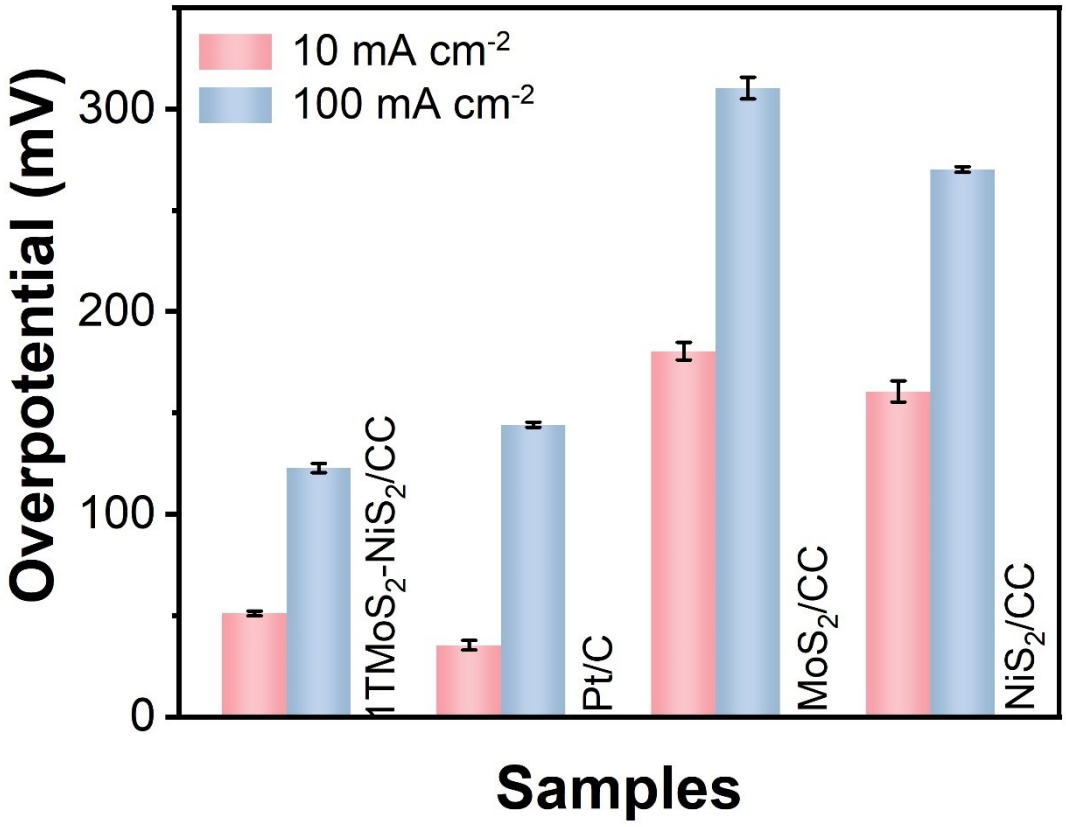

Figure S8. The corresponding overpotentials for various materials at current densities of 10 and 100 mA cm^{-2}, respectively.

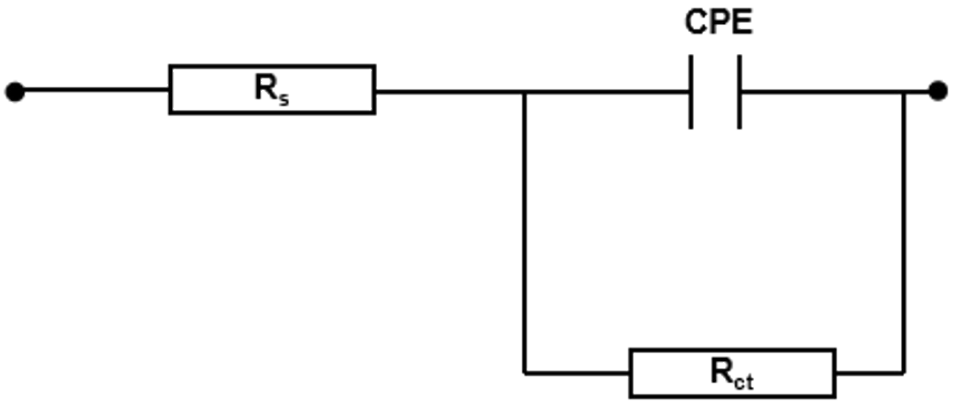

Figure S9. Equivalent circuit diagram of testing AC impedance of various materials under three electrodes.

The electrochemical active surface area (ECSA) was assessed by calculating the double-layer capacitance (C_{dl}) from cyclic voltammetry (CV) measurements at different scan rates (**Figure S10**).

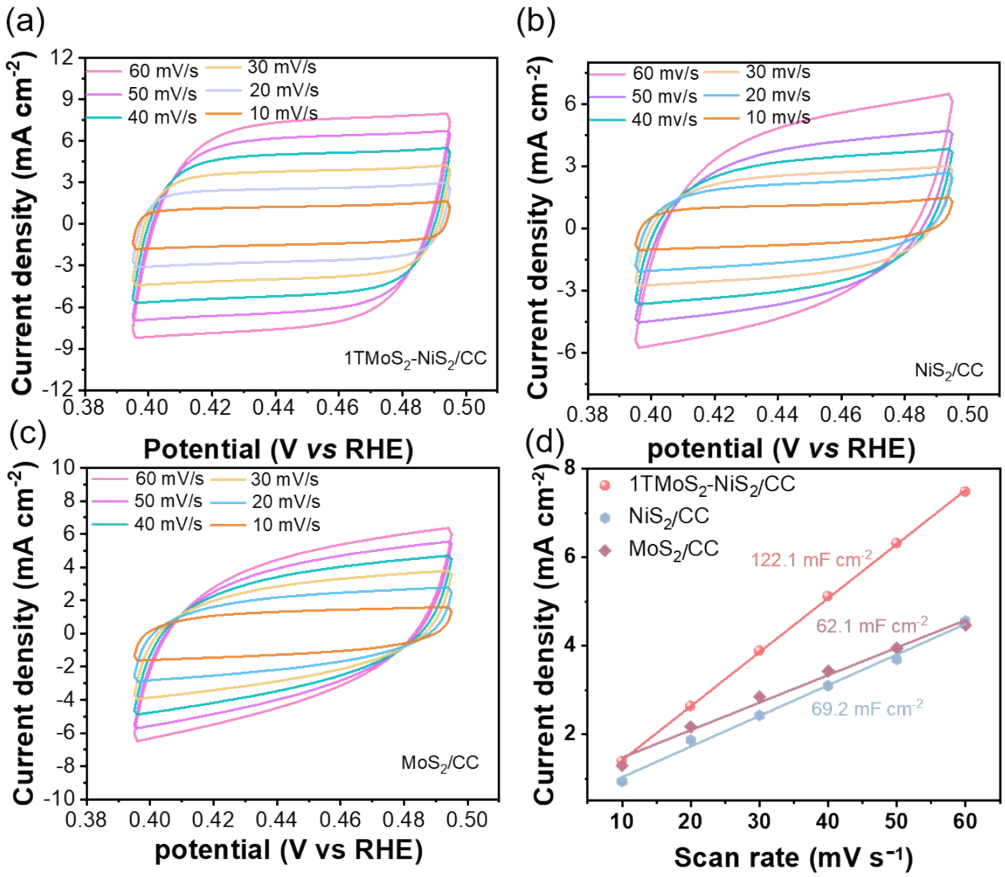

Figure S10. The CV curves of (a) $1TMoS_2$-NiS_2/CC, (b) MoS_2, and (c) NiS_2 at different scan rates from 10 to 60 mV s^{-1}. (d) C_{dl} values of various materials.

To investigate the intrinsic catalytic activity and exclude geometrical effects, the LSV curves were normalized to ECSA.

The relevant calculation formula of ECSA is as follows:

$$ECSA = \frac{C_{dl}(catalyst)\ mF\ cm^{-2}}{C_s\ mF\ cm^{-2}}$$

The specific capacitance (Cs) is value of 0.04 mF cm^{-2} to calculate the ECSA (*Nat. Commun.* **2024,** *15*, 2481). The calculated ECSA value for 1TMoS_2-NiS_2/CC was 3052.5 cm^{-2}_{ECSA}, while the ECSA values for the NiS_2/CC, and MoS_2/CC were 1730 and 1552.5 cm^{-2}_{ECSA}. This result further shows that 1TMoS_2-NiS_2/CC has excellent catalytic performance.

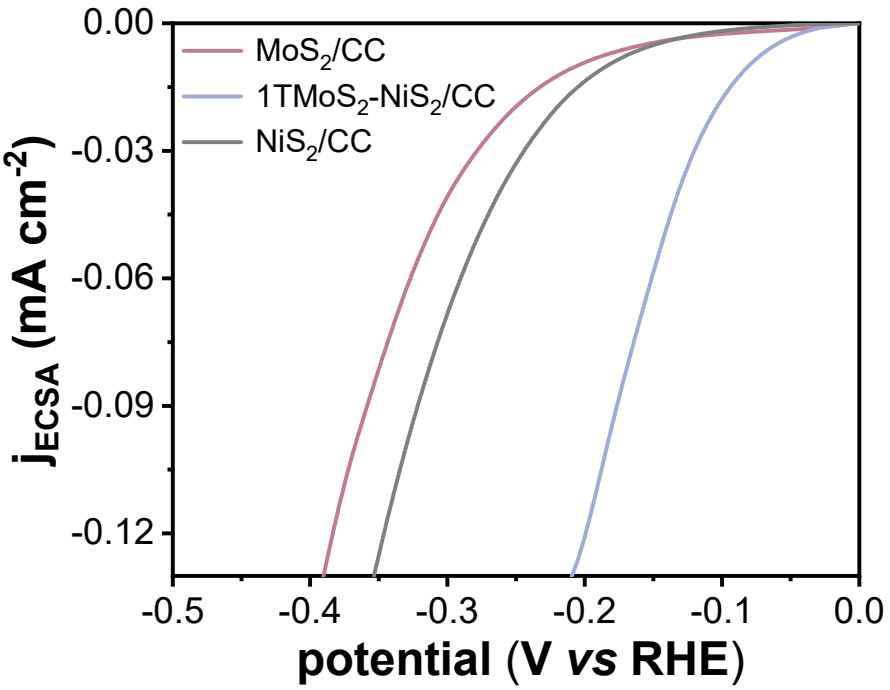

Figure S11. ECSA normalized polarization curves of 1TMoS_2-NiS_2/CC, MoS_2/CC, and NiS_2/CC.

As shown in **Figure S12a**, the HER performance of 1TMoS$_2$-NiS$_2$/CC exhibited minimal degradation when the salt concentration increased from 0 M to 5 M. At a current density of 100 mA cm^{-2}, the performance only declined by 23 mV, demonstrating notable resistance to salt corrosion. As shown in **Figure S12b**, 1TMoS$_2$-NiS$_2$/CC exhibits excellent HER performance in real seawater. The above experimental results show that the 1TMoS$_2$-NiS$_2$/CC prepared by one-step vulcanization method shows good catalyst activity in different media.

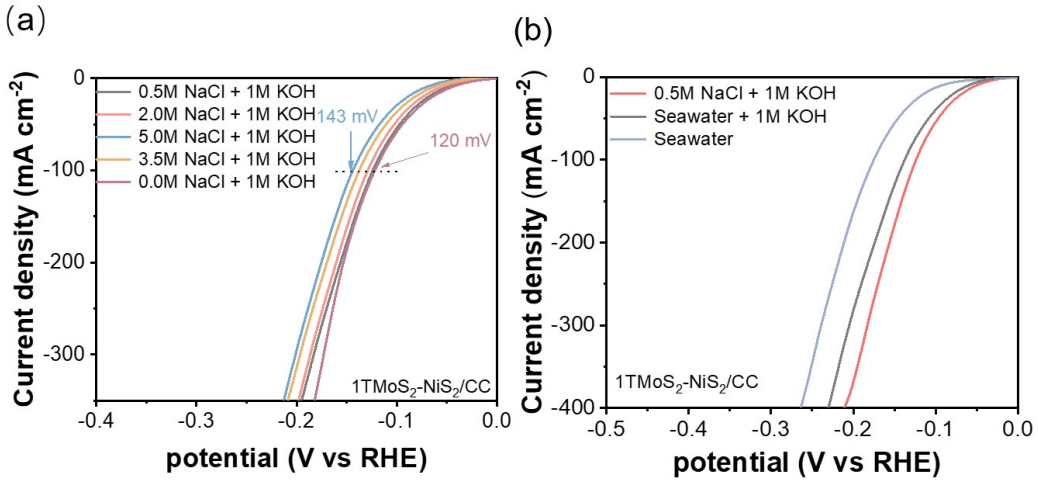

Figure S12. (a) LSV curves of 1TMoS$_2$-NiS$_2$/CC for the HER in different salt solutions, respectively. (b) LSV curves of 1TMoS$_2$-NiS$_2$/CC for the HER in various media.

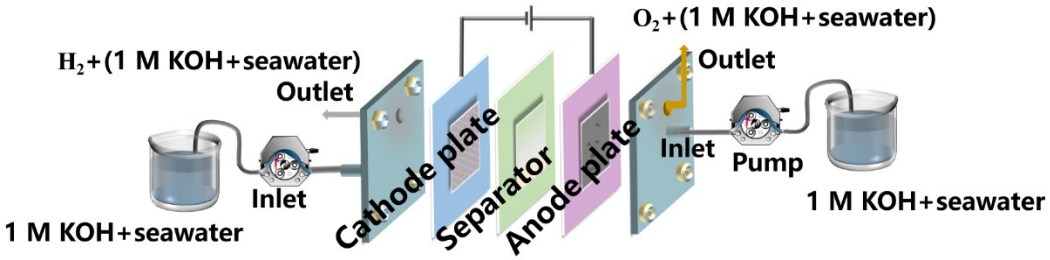

Figure S13. Schematic diagram of flow electrolytic cell.

As shown in **Figure S14**, the hydrogen production Faraday efficiency (FE) of the catalyst is 99.2% calculated by drainage method at 50 mA cm^{-2}, which shows that the catalyst thus prepared has good seawater electrolysis activity and selectivity.

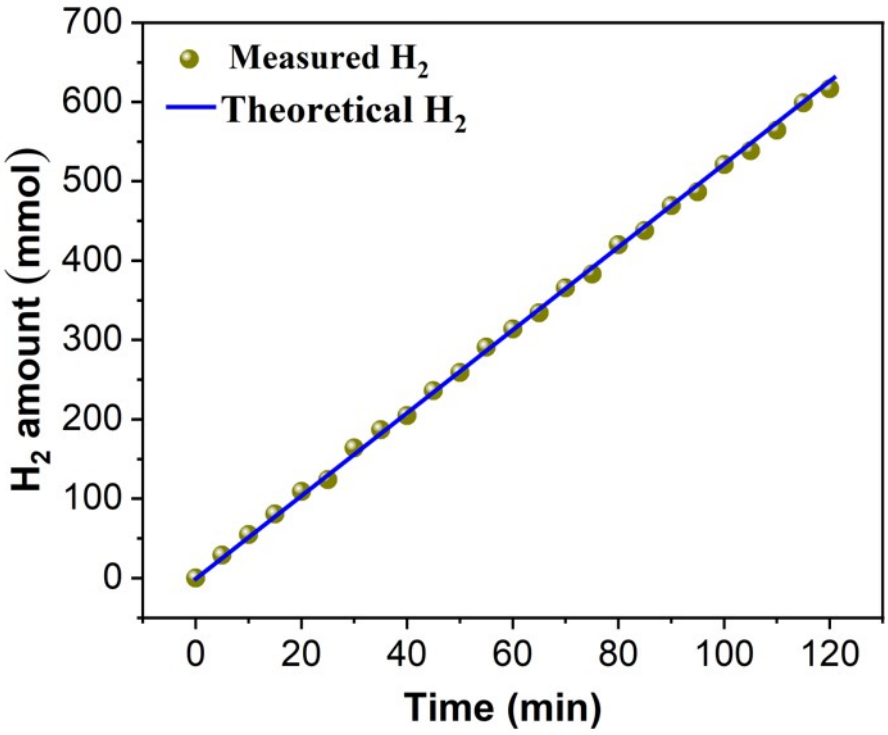

Figure S14. Faraday efficiency of producing H_2.

SEM and TEM analysis reveals that the 1TMoS$_2$-NiS$_2$/CC electrode retains its original nanosheet-modified nanoarray structure even after an extended hydrogen evolution reaction.

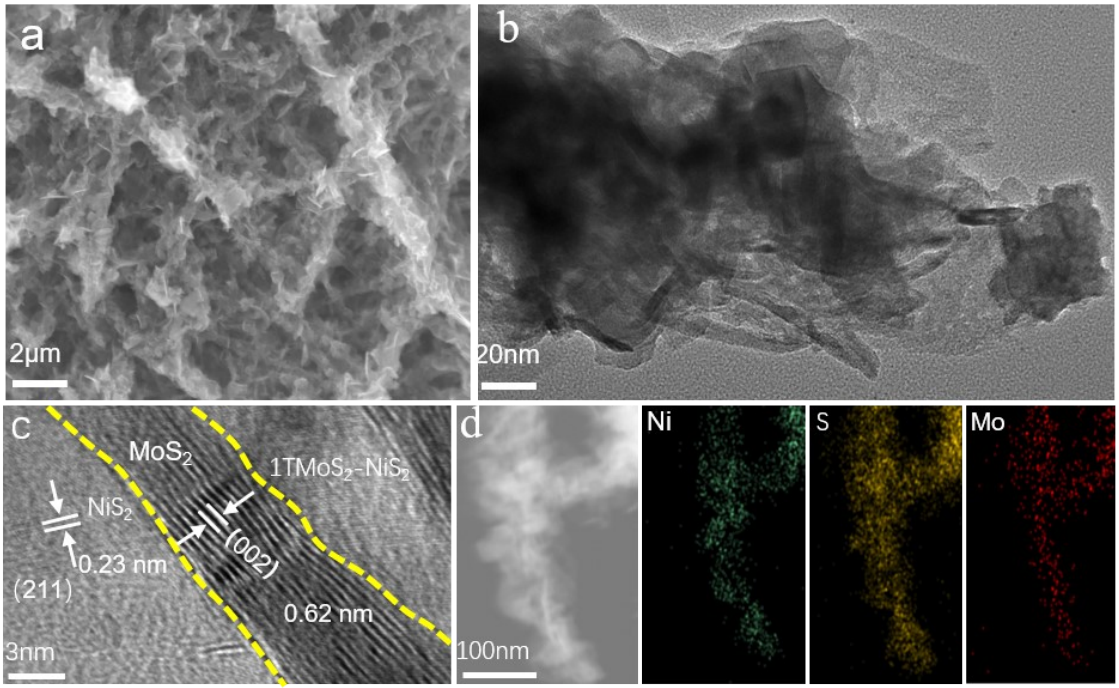

Figure S15. (a) SEM image, (b) TEM image, (c) HRTEM and (d) Elemental-mapping images of 1TMoS$_2$-NiS$_2$/CC after HER durability test.

Additionally, XRD analysis reveals that the diffraction peaks of MoS_2 and NiS_2 are unaffected after the stability test **(Figure S16)**. This further confirms the outstanding stability of the material in alkaline seawater.

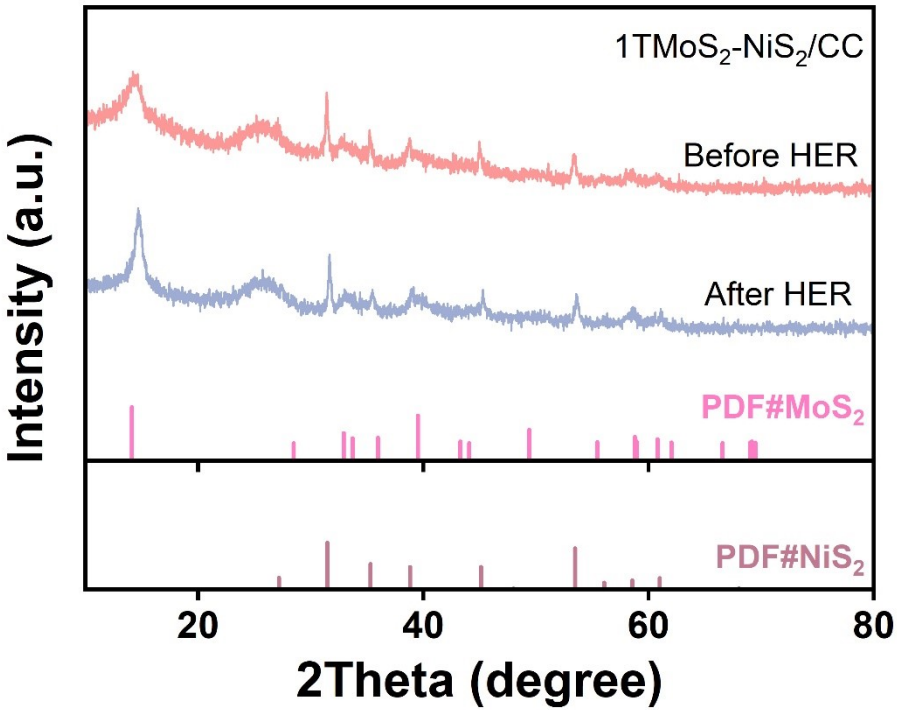

Figure S16. XRD pattern before and after HER reaction of 1TMoS$_2$-NiS$_2$/CC.

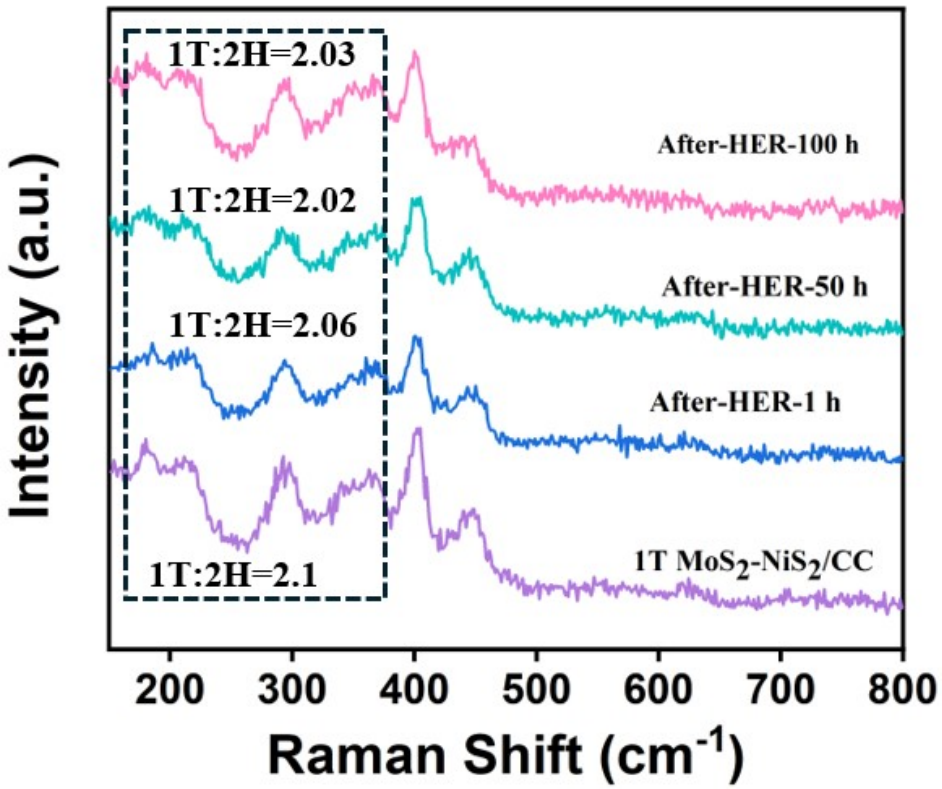

Figure S17. In-situ Raman spectra of 1TMoS$_2$-NiS$_2$/CC at different reaction times.

We directly transform the NiMoO precursor into 1TMoS_2 and NiS_2 heterojunction by a simple one-step vulcanization method. The octahedrally structured NiMoO precursor was converted in situ to octahedrally structured 1TMoS_2-NiS_2. The electrons in NiS_2 occupy the Mo 4d orbitals of 1T-MoS_2, thus maintaining the 1T phase stable (see detailed analysis in Figure 4 of the manuscript). Meanwhile, 1TMoS_2 and NiS_2 form close connection on heterogeneous interfaces and share "S bridge" atoms, which changes the coordination state of S atoms to reduce precipitation and dissolution in the catalytic process, and optimizes the absorption/desorption energy of H_{ads}, thus improving the structural stability and catalytic activity of 1T phase. However, 1TMoS_2-NiS_2/CC contains a small amount of 2HMoS_2 phase, which is easy to reconstruct and form SO_4^{2-} adsorbed on the catalyst surface (*Adv. Funct. Mater.* **2023**, *33*, 2209572), thus protecting the catalyst from seawater corrosion. It is worth noting that due to the strong electronic interaction between 1TMoS_2 and NiS_2, the structure has not changed during the catalytic process. As shown in **Figure S18**, during the HER process, when the potential reaches -0.2 V, a small broad peak appears at 900-1000 cm^{-1}, which is gradually enhanced with the increase of the potential, and this peak can be attributed to the characteristic signal of SO_4^{2-}. It is noteworthy that the characteristic peak of 1T-MoS_2 did not show any obvious weakening or disappearance throughout the reaction process (Raman spectra show characteristic peaks at 173, 215, and 351 cm^{-1}, corresponding to the J_1, J_2, and J_3 vibrational modes of 1T MoS_2), which further suggests that the catalyst maintained a stable metallic phase structure during the electrochemical process. We speculate that this phenomenon may originate from the trace amount of 2HMoS_2 phase impurities in the material (confirmed by XPS and TEM results). During the electrochemical reaction, 2HMoS_2 may undergo a local structural evolution to produce SO_4^{2-}, while the main 1T phase remains stable.

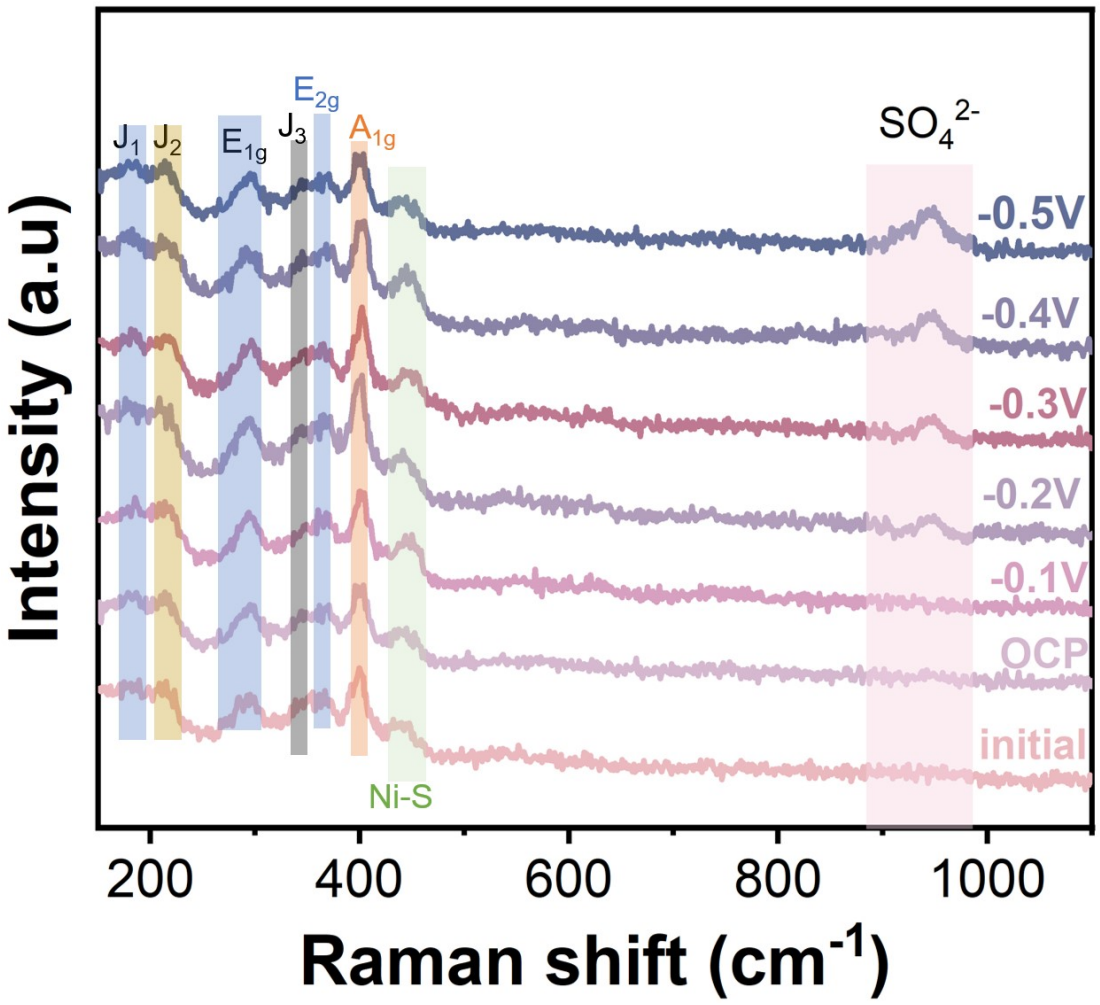

Figure S18. In-situ Raman curve of continuous hydrogen evolution of 1TMoS$_2$-NiS$_2$/CC in alkaline seawater.

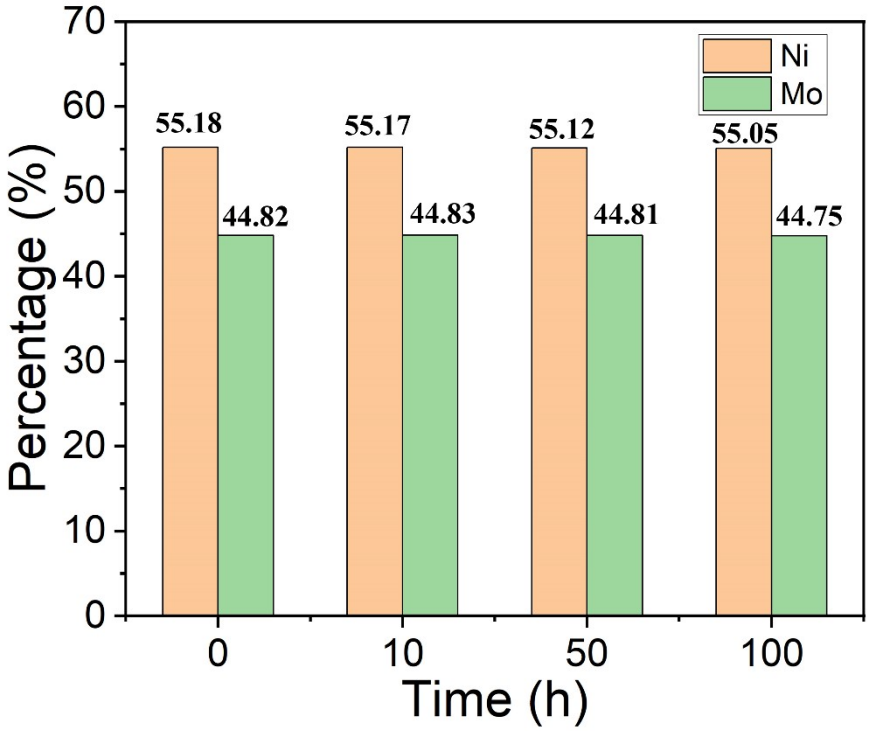

Figure S19. ICP-OES test results of 1TMoS_2-NiS_2/CC electrode at different times.

The NiMoO precursor into $1TMoS_2$ and NiS_2 heterojunction by a simple one-step vulcanization method. $1TMoS_2$-NiS_2/CC contains a small amount of $2HMoS_2$ phase, which is easy to reconstruct and form SO_4^{2-} adsorbed on the catalyst surface, thus protecting the catalyst from seawater corrosion. The experiment of calculating electric double layer (C_{dl}) by cyclic voltammetry curve after 100 h of HER. As shown in **Figure S20a, b**, compared with the CV curve before the reaction, the area of the curve after the reaction is similar. After calculation, the C_{dl} values of the two are very close (**Figure S20c**), indicating that they have the same electrochemical active area. In addition, after 3000 cycles of continuous hydrogen evolution with different current densities, it still has the same catalytic activity as the initial one (**Figure S20d**), demonstrating that the catalyst reconfiguration does not affect the catalytic activity. The above results show that the SO_4^{2-} formed after reconstruction are adsorbed on the catalyst surface, which will not affect the ion concentration on the catalyst surface and the activity of catalytic sites.

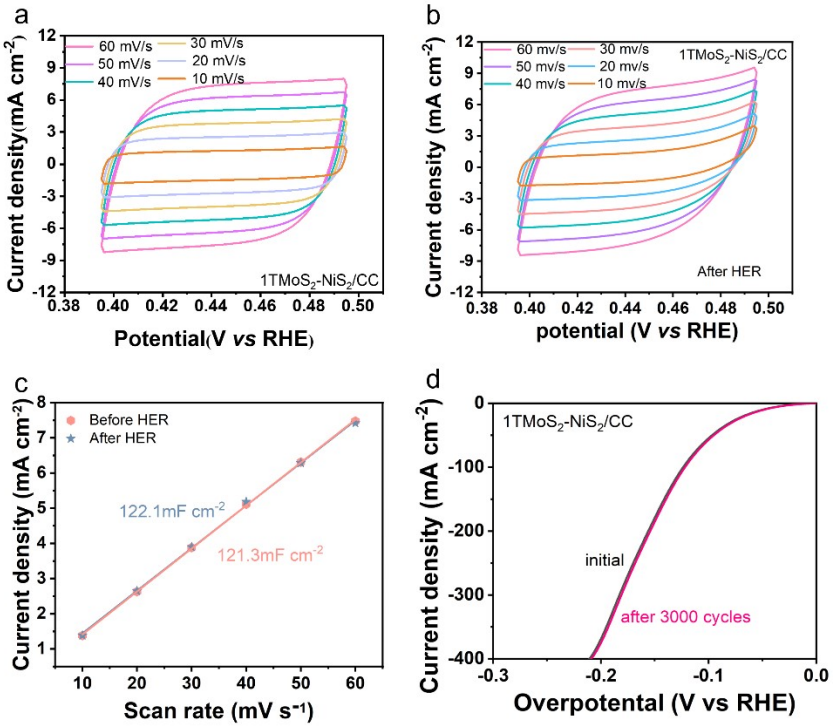

Figure S20. (a) The CV curves of $1TMoS_2$-NiS_2/CC. (b) CV curve of $1TMoS_2$-NiS_2/CC after continuous hydrogen evolution for 100 h. (d) C_{dl} values of various materials. (c) HER LSV curves of $1TMoS_2$-NiS_2/CC before (black) and after (red) 3000 CV cycles.

In contrast, 1T-MoS_2 is metallic and highly conductive, and these advantages have led 1T-MoS_2 to exhibit superior performance in catalysis and energy storage. However, the Mo 4d orbitals of 1T-MoS_2 are not completely filled and exhibit low energy levels, which are difficult to be synthesized directly, greatly limiting its further applications (*Nano Research*, 2025, *18*, 94907020). In addition, each Mo center in the two phases is surrounded by six S atoms, and the S atoms are easily reconstructed by the overpotential in HER, which leads to the loss of a large number of S components and the rapid degradation of activity (*Appl. Catal. B: Environ.* 2022, 300, 120696). We directly transform the NiMoO precursor into 1TMoS_2 and NiS_2 heterojunction by a simple one-step vulcanization method. The octahedrally structured NiMoO precursor was converted in situ to octahedrally structured 1TMoS_2-NiS_2. The electrons in NiS_2 occupy the Mo 4d orbitals of 1T-MoS_2, thus maintaining the 1T phase stable (see detailed analysis in Figure 4 of the manuscript). However, 1TMoS_2-NiS_2/CC contains a small amount of 2HMoS_2 phase, which is easy to reconstruct and form SO_4^{2-} adsorbed on the catalyst surface,[11] thus protecting the catalyst from seawater corrosion. It is worth noting that due to the strong electronic interaction between 1TMoS_2 and NiS_2, the structure has not changed during the catalytic process. As shown in **Figure S21**, the XPS spectrum of Mo3d before and after the 1TMoS_2-NiS_2/CC reaction shows that the binding energy position of the phase 2H after HER significantly shifted forward, indicating that the phase 2H participated in the reaction. Meanwhile, the decrease of content indicates that the 2H phase has been reconstructed.

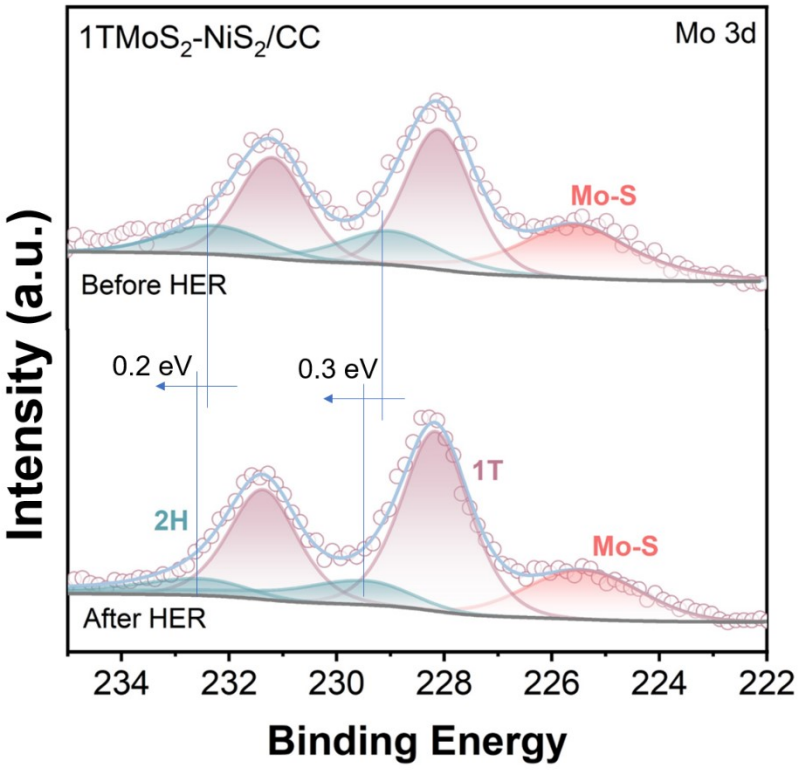

Figure S21. The XPS spectrum of Mo3d before and after the 1TMoS$_2$-NiS$_2$/CC reaction.

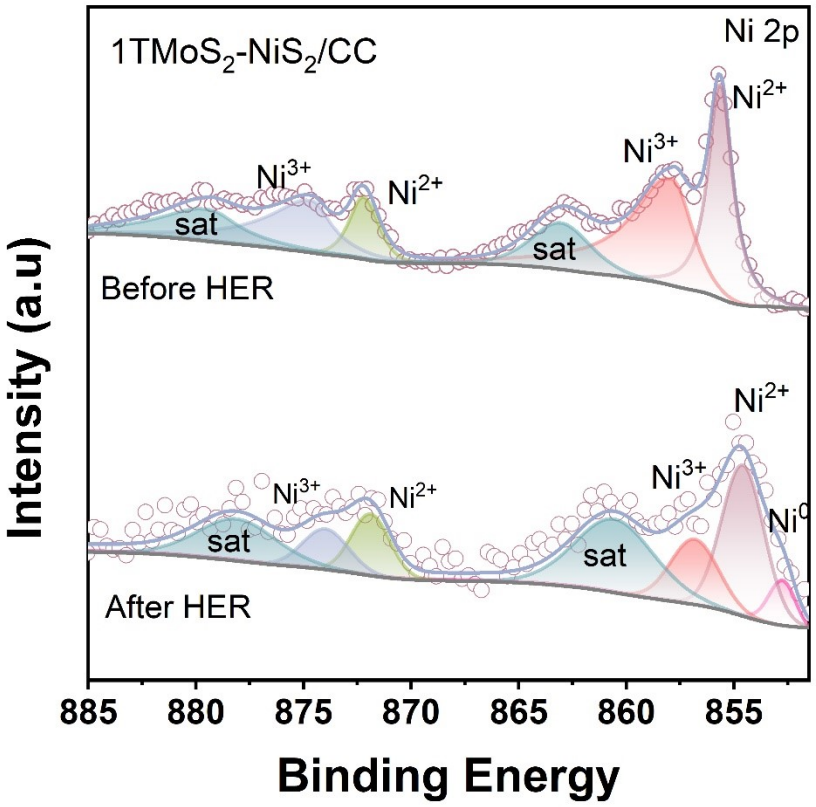

Figure S22. The XPS spectrum of Mo3d before and after the $1TMoS_2$-NiS_2/CC reaction.

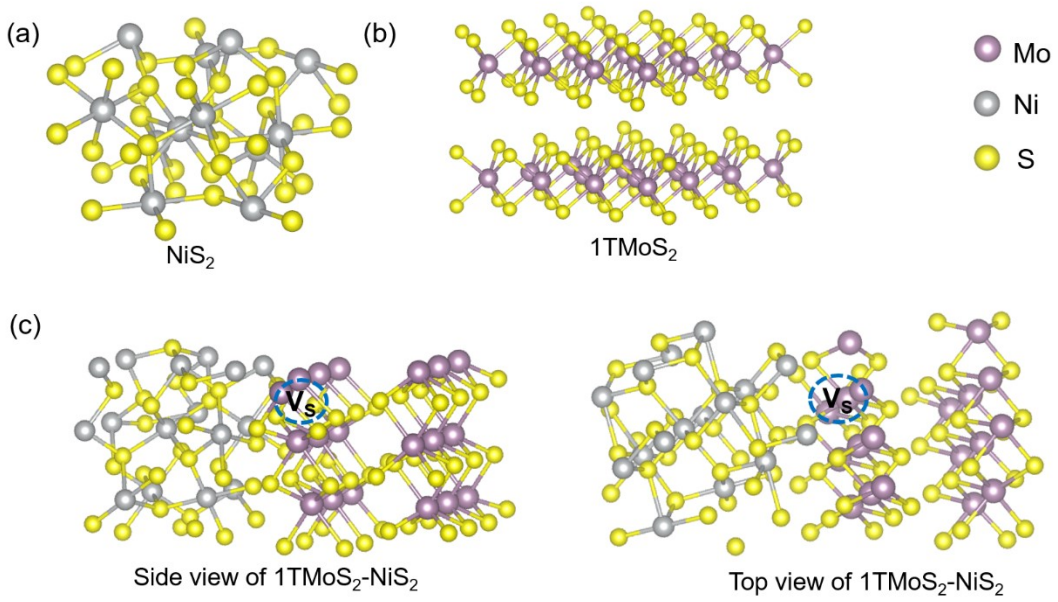

Figure S23. Theoretical calculation models for (a) NiS_2, (b) $1TMoS_2$, and (c) $1TMoS_2$-NiS_2 after optimization.

Compared to 1TMoS$_2$ and NiS$_2$, electrons initially accumulate at the Mo and Ni sites (**Figure S24**).

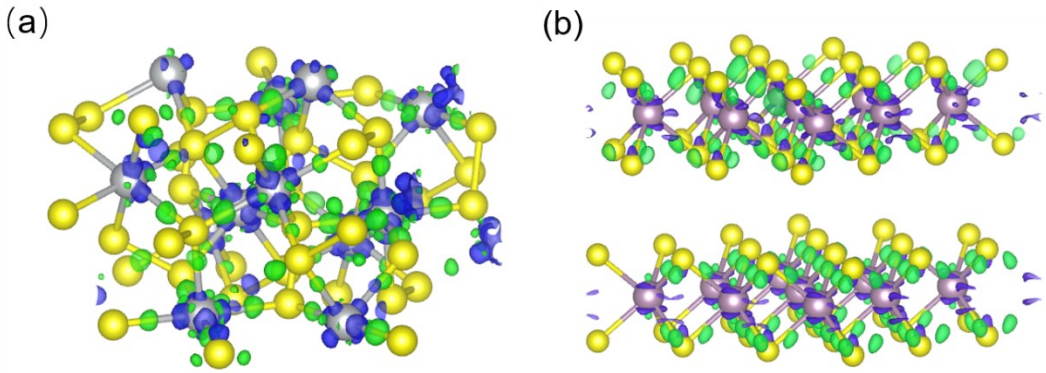

Figure S24. Charge density differential image of NiS$_2$ and 1TMoS$_2$ (without adsorbed H$_2$O). Purple, yellow and gray represent Mo, S and Ni atoms respectively. Blue represents the concentration of electrons, green represents the dissipation of electrons.

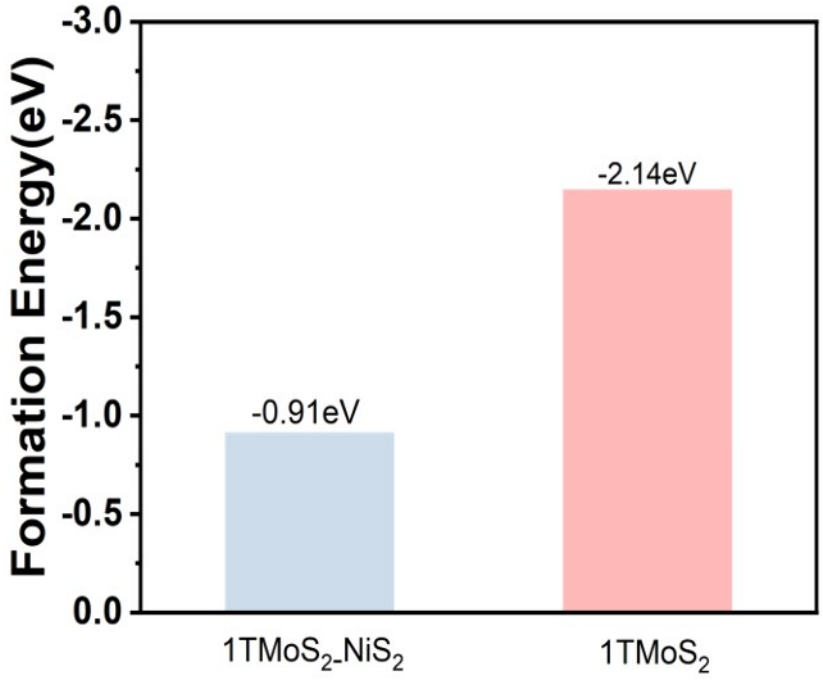

Figure S25. The formation energy of $1TMoS_2$ and $1TMoS_2$-NiS_2. (c) The DOS curves of $1TMoS_2$-NiS_2/CC and $1TMoS_2$.

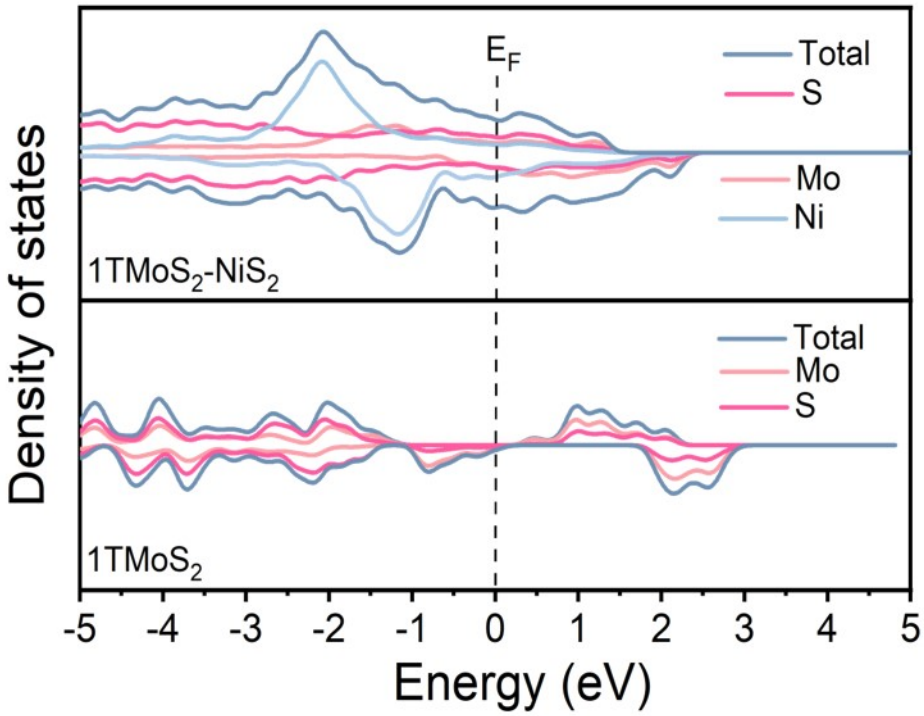

Figure S26. The DOS curves of various materials.

The side view and top view models of adsorbed water molecules after the interface of $1TMoS_2$-NiS_2/CC is reconstructed to form SO_4^{2-} (named $1TMoS_2$-NiS_2/CC-after) were observed from different angles.

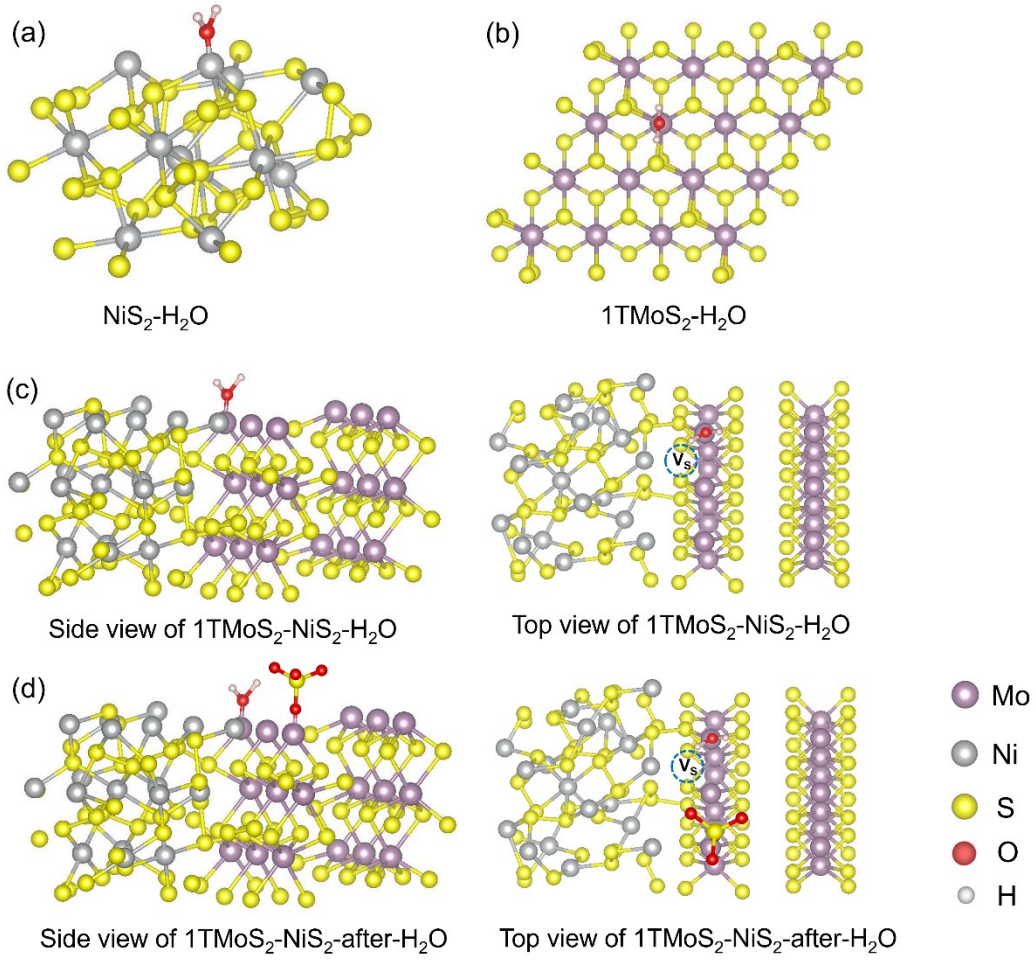

Figure S27. Theoretical model of H_2O adsorption at different sites of (a) NiS_2, (b) $1TMoS_2$. (c) $1TMoS_2$-NiS_2/CC and (d) $1TMoS_2$-NiS_2/CC-after for adsorbing water molecules (Mo-H_2O) were observed from different angles.

The introduction of NiS_2 effectively modifies the electronic state of Mo atoms in $1TMoS_2$, favoring the formation of Mo-H bonds over S-H bonds during hydrogen evolution. This modification also accelerates the dissociation of Mo-H, indicates faster Volmer processes.

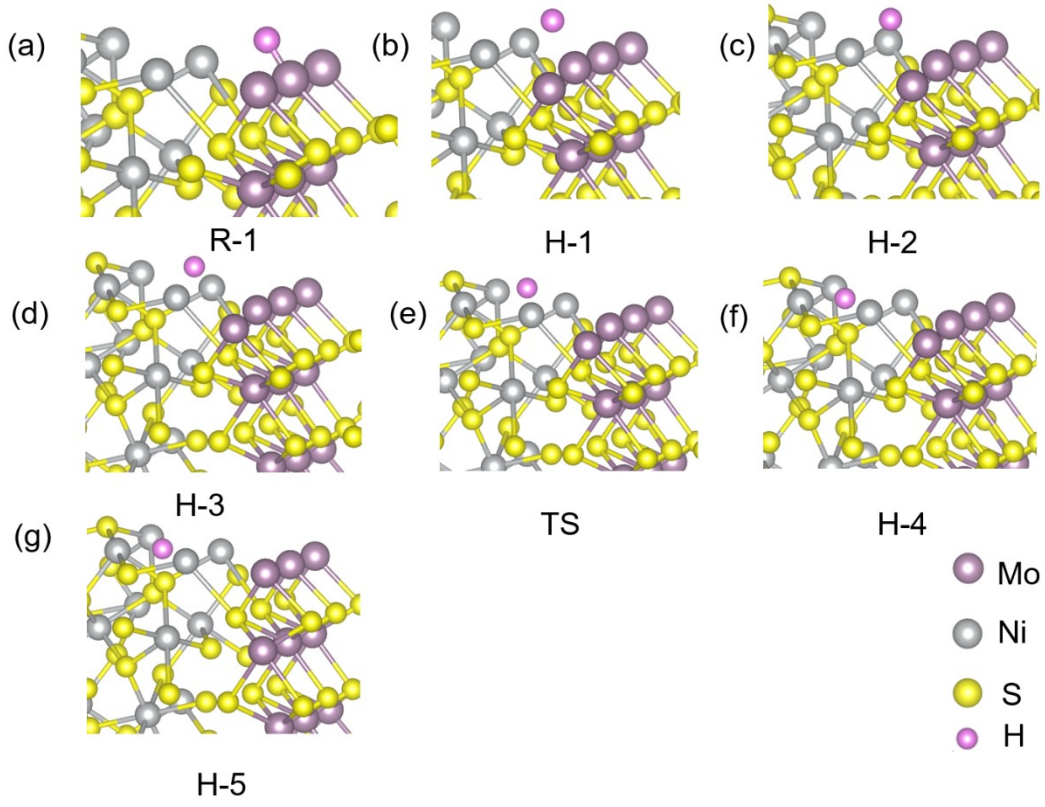

Figure 28. To reveal the actual active sites, we compared the energies of H*absorption and dissociation on a series of possible active sites of the $1TMoS_2$-NiS_2 nanosheets. (a-g) Based on the atomic configurations of the $1TMoS_2$-NiS_2 nanosheets, six different sites for H* absorption were considered. R-1 represents the adsorption of H* to the Mo site. Ts stands for transition state.

Table S1. EXAFS data fitting results of Samples.

Sample	Path	*CN*[a]	*R*(Å)[b]	σ^2 (Å^2)[c]	ΔE_0(eV)[d]	*R* factor
Mo K-edge (S_0^2=0.877)						
Mo foil	Mo-Mo	8.0*	2.715±0.004	0.0039	3.4±1.0	0.0026
	Mo-Mo	6.0*	3.130±0.006			
MoS2	Mo-S	6.4±0.2	2.404±0.003	0.0026	-0.3±0.8	0.0072
	Mo-S-Mo	6.1±0.2	3.169±0.003	0.0039		
1TMoS$_2$-NiS$_2$/CC	Mo-S	6.0±0.1	2.402±0.002	0.0028	3.1±0.5	0.0045
	Mo-S-Mo	3.9±0.2	3.160±0.002	0.0039		

Table S2. Comparison of the HER performance of $1TMoS_2$-NiS_2/CC with the state-of-the-art electrocatalysts reported.

Samples	Electrolyte	η_{100} (mV) (j=100 mA cm^{-2})	Ref.
$1TMoS_2$-NiS_2/CC	**1 M KOH+seawater**	**138**	**This work**
NiTe@FeOOH	1 M KOH + seawater	279	[1]
P-Fe_3O_{4-X}	1 M KOH + seawater	210	[2]
NiFeS/NF	1 M KOH + seawater	217	[3]
CoPx/NF	1 M KOH + seawater	190	[4]
Ni_2P-Fe_2P/NF	1 M KOH + seawater	252	[5]
Ni-SN@C	1 M KOH + seawater	180	[6]
Co_xP_v@NC	1 M KOH + seawater	158	[7]
S-$NiMoO_4$@NiFe-LDH	1 M KOH + seawater	222	[8]
Co-$MoSe_2$	1 M KOH + seawater	190	[9]
NiPS/NF	1 M KOH + seawater	188	[10]
NiFe-P@NC	1 M KOH + seawater	153	[11]
NRAHM-NiO/NF	1 M KOH + seawater	340	[12]
NiCoP/NF	1 M KOH + seawater	171	[13]
MnCo/NiSe/NF	1 M KOH + seawater	202	[14]
RuNi-Fe_2O_3/IF	1 M KOH + seawater	150	[15]
Co-P@NN	1 M KOH + seawater	245	[16]
B-NiCoP	1 M KOH + seawater	223	[17]

Table S3. Comparison of the overall water splitting performance of 1TMoS$_2$-NiS$_2$/CC||RuO$_2$/CC with the state-of-the-art electrocatalysts reported so far electrolyte.

Samples	Cell voltage (V) (j=100mA cm^{-2})	electrolyte	Ref.
1TMoS$_2$-NiS$_2$/CC	**1.67**	**1M KOH+0.5M NaCl**	**This work**
S-NiMoO4@NiFe-LDH	1.68	1M KOH+0.5M NaCl	18
NiCoS@NiMoS	1.72	1M KOH+0.5M NaCl	19
Cu$_2$O@Ni	1.72	1M KOH+0.5M NaCl	20
Co-Fe$_2$P	1.69	1 M KOH + 0.5M NaCl	21
Ni-SN@C	1.72	1 M KOH + Seawater	22
GO@Fe@NiCo/NF	1.8	1M KOH+0.5M NaCl	23
Mo-CoP$_X$/NF	2.16	1 M KOH + Seawater	24
F-FeCoP$_v$@IF	1.7	1 M KOH + Seawater	25
NiCoHPi@Ni$_3$N/NF	1.95	1 M KOH + Seawater	26
Cr-Co$_x$P	1.85	1 M KOH+seawater	27
Ni-MoO$_2$/NF	1.72	1M KOH+0.5M NaCl	28
NiFe LDH/FeOOH	2.0	1M KOH+0.5M NaCl	29

References

(1) Gao, X.; Chen, J.; Yu, Y.; Wang, F.; Wu, X.; Wang, X.; Mao, W.; Li, J.; Huang, W.; Chen, Q.; et al. Core-shell structured NiTe@FeOOH nanoarrays for efficient overall seawater splitting. *Chem. Eng. J.* **2023**, *474*, 145568.

(2) Yu, Q.; Fu, Y.; Liu, Z.; Liu, X.; Guo, L.; Wang, T.; Chi, J.; Wu, Z.; Wang, L. Regulating local atomic environment of Fe_3O_4 to promote anion exchange membrane based alkaline seawater electrolysis. *Appl. Catal. B Environ.* **2025**, *361*, 124598.

(3) Chen, J.; Zhang, L.; Li, J.; He, X.; Zheng, Y.; Sun, S.; Fang, X.; Zheng, D.; Luo, Y.; Wang, Y.; et al. High-efficiency overall alkaline seawater splitting: using a nickel–iron sulfide nanosheet array as a bifunctional electrocatalyst. *J. Mater. Chem.* **2023**, *11*, 1116-1122.

(4) Wu, L.; Yu, L.; McElhenny, B.; Xing, X.; Luo, D.; Zhang, F.; Bao, J.; Chen, S.; Ren, Z. Rational design of core-shell-structured CoP@FeOOH for efficient seawater electrolysis. *Appl. Catal. B Environ.* **2021**, *294*, 120256.

(5) Wu, L.; Yu, L.; Zhang, F.; McElhenny, B.; Luo, D.; Karim, A.; Chen, S.; Ren, Z. Heterogeneous Bimetallic Phosphide Ni_2P-Fe_2P as an Efficient Bifunctional Catalyst for Water/Seawater Splitting. *Adv. Funct. Mater.* **2021**, *31*, 2006484.

(6) Jin, H.; Wang, X.; Tang, C.; Vasileff, A.; Li, L.; Slattery, A.; Qiao, S. Z. Stable and Highly Efficient Hydrogen Evolution from Seawater Enabled by an Unsaturated Nickel Surface Nitride. *Adv Mater* **2021**, *33*, 2007508.

(7) Wang, X.; Liu, X.; Wu, S.; Liu, K.; Meng, X.; Li, B.; Lai, J.; Wang, L.; Feng, S. Phosphorus vacancies enriched cobalt phosphide embedded in nitrogen doped carbon matrix enabling seawater splitting at ampere-level current density. *Nano Energy* **2023**, *109*, 108292.

(8) Wang, H.; Chen, L.; Tan, L.; Liu, X.; Wen, Y.; Hou, W.; Zhan, T. Electrodeposition of NiFe-layered double hydroxide layer on sulfur-modified nickel molybdate nanorods for highly efficient seawater splitting. *J. Colloid Interface Sci.* **2022**, *613*, 349-358.

(9) Xu, Y.; Fo, Y.; Lv, H.; Cui, X.; Liu, G.; Zhou, X.; Jiang, L. Anderson-Type Polyoxometalate-Assisted Synthesis of Defect-Rich Doped 1T/2H-$MoSe_2$ Nanosheets for Efficient Seawater Splitting and Mg/Seawater Batteries. *ACS Appl Mater Interfaces* **2022**, *14*, 10246-10256.

(10) Wang, H.-Y.; Ren, J.-T.; Wang, L.; Sun, M.-L.; Yang, H.-M.; Lv, X.-W.; Yuan, Z.-Y. Synergistically enhanced activity and stability of bifunctional nickel phosphide/sulfide heterointerface electrodes for direct alkaline seawater electrolysis. *J. Energy Chem.* **2022**, *75*, 66-73.

(11) Chen, Z.; Li, Q.; Xiang, H.; Wang, Y.; Yang, P.; Dai, C.; Zhang, H.; Xiao, W.; Wu, Z.; Wang, L. Hierarchical porous NiFe-P@NC as an efficient electrocatalyst for alkaline hydrogen production and seawater electrolysis at high current density. *Inorg. Chem. Front.* **2023**, *10*, 1493-1500.

(12) Hemmati, K.; Kumar, A.; Jadhav, A. R.; Moradlou, O.; Moshfegh, A. Z.; Lee, H. Nanorod Array-Based Hierarchical NiO Microspheres as a Bifunctional Electrocatalyst for a Selective and Corrosion-Resistance Seawater Photo/Electrolysis System. *ACS Catal.* **2023**, *13*, 5516-5528.

(13) Nguyen, C. N.; Tran, T. T. N.; Truong, T.-K.; Le, T. A.; Le, T. N.-M.; Nguyen, L. H. T.; Nguyen, C. C.; Tran, N. Q. MOF-Templated Synthesis of Three-Dimensional B-Doped NiCoP Hollow Nanorod Arrays for Highly Efficient and Stable Natural Seawater Splitting. *ACS Appl. Energy Mater.* **2023**, *6*, 10713-10722.

(14) Andaveh, R.; Sabour Rouhaghdam, A.; Ai, J.; Maleki, M.; Wang, K.; Seif, A.; Barati Darband, G.; Li, J. Boosting the electrocatalytic activity of NiSe by introducing MnCo as an efficient heterostructured

electrocatalyst for large-current-density alkaline seawater splitting. *Appl. Catal. B Environ.* **2023**, *325*, 122355.
(15) Cui, T.; Zhai, X.; Guo, L.; Chi, J.-Q.; Zhang, Y.; Zhu, J.; Sun, X.; Wang, L. Controllable synthesis of a self-assembled ultralow Ru, Ni-doped Fe_2O_3 lily as a bifunctional electrocatalyst for large-current-density alkaline seawater electrolysis. *Chin. J. Catal.* **2022**, *43*, 2202-2211.
(16) Liang, R.; Fan, J.; Lei, F.; Li, P.; Fu, C.; Lu, Z.; Hao, W. Fabrication of ultra-stable and high-efficient CoP-based electrode toward seawater splitting at industrial-grade current density. *J Colloid Interface Sci* **2023**, *645*, 227-240.
(17) He, L.; Cai, Z.; Zheng, D.; Ouyang, L.; He, X.; Chen, J.; Li, Y.; Guo, X.; Liu, Q.; Li, L.; et al. Three-dimensional porous NiCoP foam enabled high-performance overall seawater splitting at high current density. *J. Mater. Chem.* **2024**, *12*, 2680-2684.
(18) Wang, C.; Zhu, M.; Cao, Z.; Zhu, P.; Cao, Y.; Xu, X.; Xu, C.; Yin, Z. Heterogeneous bimetallic sulfides based seawater electrolysis towards stable industrial-level large current density. *Appl. Catal. B Environ.* **2021**, *291*, 120071.
(19) Zhang, B.; Xu, W.; Liu, S.; Chen, X.; Ma, T.; Wang, G.; Lu, Z.; Sun, J. Enhanced interface interaction in Cu_2S@Ni core-shell nanorod arrays as hydrogen evolution reaction electrode for alkaline seawater electrolysis. *J. Power Sources* **2021**, *506*, 230235.
(20) Wang, S.; Yang, P.; Sun, X.; Xing, H.; Hu, J.; Chen, P.; Cui, Z.; Zhu, W.; Ma, Z. Synthesis of 3D heterostructure Co-doped Fe_2P electrocatalyst for overall seawater electrolysis. *Appl. Catal. B Environ.* **2021**, *297*, 120386.
(21) Jadhav, A. R.; Kumar, A.; Lee, J.; Yang, T.; Na, S.; Lee, J.; Luo, Y.; Liu, X.; Hwang, Y.; Liu, Y.; et al. Stable complete seawater electrolysis by using interfacial chloride ion blocking layer on catalyst surface. *J. Mater. Chem. A* **2020**, *8*, 24501-24514.
(22) Yu, Y.; Li, J.; Luo, J.; Kang, Z.; Jia, C.; Liu, Z.; Huang, W.; Chen, Q.; Deng, P.; Shen, Y.; et al. Mo-decorated cobalt phosphide nanoarrays as bifunctional electrocatalysts for efficient overall water/seawater splitting. *Mater. Today Nano* **2022**, *18*, 100216.
(23) Zhu, J.; Chi, J.; Cui, T.; Guo, L.; Wu, S.; Li, B.; Lai, J.; Wang, L. F doping and P vacancy engineered FeCoP nanosheets for efficient and stable seawater electrolysis at large current density. *Appl. Catal. B Environ.* **2023**, *328*, 122487.
(24) Sun, H.; Sun, J.; Song, Y.; Zhang, Y.; Qiu, Y.; Sun, M.; Tian, X.; Li, C.; Lv, Z.; Zhang, L. Nickel-Cobalt Hydrogen Phosphate on Nickel Nitride Supported on Nickel Foam for Alkaline Seawater Electrolysis. *ACS Appl. Mater. Interfaces.* **2022**, *14*, 22061-22070.
(25) Song, Y.; Sun, M.; Zhang, S.; Zhang, X.; Yi, P.; Liu, J.; Huang, B.; Huang, M.; Zhang, L. Alleviating the Work Function of Vein-Like Co_XP by Cr Doping for Enhanced Seawater Electrolysis. *Adv. Funct. Mater.* **2023**, *33*, 2214081.
(26) Xiong, G.; Chen, Y.; Zhou, Z.; Liu, F.; Liu, X.; Yang, L.; Liu, Q.; Sang, Y.; Liu, H.; Zhang, X.; et al. Rapid Synthesis of Various Electrocatalysts on Ni Foam Using a Universal and Facile Induction Heating Method for Efficient Water Splitting. *Adv. Funct. Mater.* **2021**, *31*, 2009580.
(27) Jiang, K.; Liu, W.; Lai, W.; Wang, M.; Li, Q.; Wang, Z.; Yuan, J.; Deng, Y.; Bao, J.; Ji, H. NiFe Layered Double Hydroxide/FeOOH Heterostructure Nanosheets as an Efficient and Durable Bifunctional Electrocatalyst for Overall Seawater Splitting. *Inorg. Chem.* **2021**, *60*, 17371-17378.